



Characterization of Shale Softening by Large Volume-Based Nanoindentation

Yunhu Lu^{1,2} · Yucheng Li³ · Yongkang Wu³ · Shengmin Luo³ · Yan Jin^{1,2} · Guoping Zhang³ 

Received: 12 June 2019 / Accepted: 19 September 2019 / Published online: 19 October 2019
© Springer-Verlag GmbH Austria, part of Springer Nature 2019

Abstract

A novel statistical nanoindentation technique is presented that obtains massive data on the basis of shale sample's large volume (LV) to assess water-induced softening in terms of Young's moduli of both individual minerals at the micro/nano-scale and the bulk rock at the macroscale, with the latter extracted by a newly proposed surround effect model. Distinguished from traditional statistical nanoindentation that only examines the material at shallow depths of up to a few micrometers, this LV-based method obtains successive measurements to much larger depths of up to ~300 μm via sacrificial removal of the previously indented surface layer, enabling assessment of changes in mechanical properties over a large volume. Natural shale sample was first hydrothermally treated to cause softening, followed by statistical indentation with continuous stiffness measurement (CSM) on successive layers of increasing depth upon removal by polishing of the prior tested layers. For each tested surface, cumulative distribution function (CDF)-based deconvolution was performed to analyze multiple subsets of the massive data (i.e., ~1000 curves), each of which was extracted from the CSM curves via segmentation at a fixed depth. Such results on different segmentation depths were then fitted by the surround effect model to extract the Young's modulus of individual minerals and bulk rock. The clay matrix is highly sensitive to rock–water interactions and its Young's modulus decreases significantly from 29.2 to 16.5 GPa upon 30 days' treatment. The average rate of softening advancement was estimated to be ~10.5 μm/day, suggesting that softening advancement is intrinsically controlled by permeability, despite various physical and chemical softening mechanisms.

Keywords Large volume · Nanoindentation · Shale softening · Statistical deconvolution · Surround effect

1 Introduction

With the ever-increasing demand for cleaner fuels and development of technologies for shale gas recovery (e.g., hydraulic fracturing, horizontal drilling), the supply and consumption of shale gas play a vital role in economy, environmental protection, and energy security (Giger et al. 1984). In the petroleum industry, hydraulic fracturing, a widely used key technology for improved extraction of oil and gas from shales and other tight formations (King 2012; Lu et al. 2019), is usually assisted or enhanced by other stimulation techniques to keep pre-existing fractures open and further create new extensive fracture networks for easy permeation of oil and gas in tight rocks. In general, mainly because of the environmental and economic concerns, water-based hydraulic fracturing fluids are used, but they are also loaded with various chemical stimulants (e.g., acid) and additives (e.g., guar gum, proppants) for enhancing and improving oil and gas recovery rate, maintaining wellbore

Yunhu Lu and Yucheng Li equally contributed to this article.

✉ Yan Jin
jiny@cup.edu.cn

✉ Guoping Zhang
zhangg@umass.edu; gzhang@alum.mit.edu

¹ State Key Laboratory of Petroleum Resources and Prospecting, China University of Petroleum (Beijing), Beijing 102249, China

² College of Petroleum Engineering, China University of Petroleum (Beijing), Beijing 102249, China

³ Department of Civil and Environmental Engineering, University of Massachusetts Amherst, Amherst, MA 01003, USA

stability, minimizing well deterioration, and even preventing damage to the reservoirs. As such, extensive fluid–chemical–rock interactions may take place during various stages of operation, including initial drilling, subsequent hydraulic fracturing, stimulation treatments, and actual hydrocarbon extraction processes.

Shale is a multiphase, porous, sedimentary rock or composite material mainly consisting of naturally occurring inorganic solid minerals (e.g., quartz, calcite, pyrite, and clay minerals) and organic matter (e.g., kerogens). It is well recognized that some of the solid minerals can be involved in primarily chemical reactions and secondarily physical interactions with the hydraulic fracturing fluids and the additives therein, such as dissolution and degradation of carbonate-based cementation (Sun et al. 2016), oxidation of pyrite and the resulting formation of acid (Rimstidt and Vaughan 2003; Chandra and Gerson 2010), and hydration and swelling of clay minerals (Chenevert 1970; Anderson et al. 2010), among others. These reactions and interactions are in fact regarded as the basic factors influencing the mechanical properties of both the bulk rock and its individual constituent minerals, some of which may become significant and even dominant in deep underground with elevated temperatures and pressures. As such, implementation of hydraulic fracturing for shale gas recovery still faces some challenges. One of the most critical issues is that the permeability of the fracture networks may decrease significantly shortly after extraction commences (e.g., 6–12 months), as indicated by a dramatic decrease in the daily production rate (Baihly et al. 2010). To date, an array of mechanisms that may lead to the decrease in fracture permeability, including unloading-induced swelling of the bulk rock (Pimentel 2003), fines migration (Pope et al. 2009), proppant diagenesis (LaFollette and Carman 2010), proppant crushing (Terracina et al. 2010), and proppant embedment (Huitt and Mcglothlin Jr. 1958), among others, has been identified and studied to various extents. For instance, a widely recognized hypothesis for the rapid reduction in shale gas production rate is that the fine-grained, negatively charged clay minerals in shales can interact with fracturing fluids, particularly water carrying the dissolved cations, via processes such as hydration, diffusion, absorption, adsorption, and permeation, leading to the swelling and softening of the clay matrix as well as the bulk rock (Du et al. 2018), which in turn causes significant proppant embedment and hence reduction in fracture permeability (Baihly et al. 2010), especially in clay-rich shales (Alramahi and Sundberg 2012). As a result, the hydraulically induced fracture networks are negatively impacted by shale softening. Therefore, to minimize this impact and maximize the long-term production of hydrocarbons from shale reservoirs, understanding the complex physical and chemical interactions between the solid minerals and fracturing fluids,

as well as pertinent consequences (i.e., softening), is of key importance to the oil and gas industry.

Traditional macroscopic measurements (e.g., uniaxial compression, triaxial testing) have been adopted to study the softening behavior of intact shale cores (Minh et al. 2004; Lin and Lai 2013), and results indicate that their mechanical properties are obviously altered by rock–fluid interactions. However, macroscopic element testing can only yield the mechanical properties, averaged on all solid phases, of the bulk rock mass, but is not capable of unveiling the mechanisms behind the complex rock–fluid interactions, nor the thickness of the softened layer. For instance, hydration and softening of the rock usually commence from the exterior surfaces, yet the effect of a thin softened layer on the exterior of a standard-sized triaxial specimen on its strength may not be readily discerned from those of other factors such as sample variability, pre-existing microcracks or joints, or other experimental errors. Over the past 2 decades, with the emergence of nanoindentation, an instrumented, nondestructive indentation technique, the mechanical properties of a variety of materials at the micro- to nano-meter scales can be probed (Oliver and Pharr 1992, 2004). Recently, nanoindentation has been extended from monolithic materials to multiphase composites, particularly those with solid inclusions, to characterize the in situ mechanical properties of individual phases within the composites (Ulm and Abou-sleiman 2006; Bobko and Ulm 2008; Bennett et al. 2015; Yang et al. 2018). In fact, using a grid indentation technique (Constantinides et al. 2006), the insights into the mechanical properties of individual phases of composite materials (e.g., shale, concrete) with solid inclusions can be uncovered on even miniature specimens of small sizes or volumes. However, this technique still has some limitations (e.g., insufficient experimental data for statistical analysis, only one specific indentation depth for the entire measurements), and hence the examined sample volume is still relatively small. Therefore, it is of significant practical importance to develop a new nanoindentation technique that can be implemented as an efficient tool for the study of mechanical properties of both the individual phases and bulk rock of shales, especially for characterization of the microscopic softening behavior of shales resulting from fluid–chemical–rock interactions.

In reality, fluid–rock interactions initially commence in the fractures, with the fluid front gradually advancing from the surfaces into the interior through the inherent nano/micropore systems of the shale. As such, the mechanical properties of the softened shale may vary with depth or the distance from the rock–fluid interface (i.e., the fracture planes), since the rock may experience different degrees of softening reactions at different depths (Wong 1998; Valès et al. 2004; Khodja et al. 2010; Guo et al. 2012; Zhou et al. 2016; Lu et al. 2019). Hence, it is of great significance to study the shale softening behavior on the basis of a large volume or depth, enabling the

assessment of gradient changes in the mechanical properties over depth (i.e., the profile of the mechanical properties over depth). Moreover, if a series of measurements can be conducted on identical samples subject to different durations of softening reactions, then it becomes feasible to estimate the rate of softening advancement (i.e., how fast the softening process advances inside the shale). In this paper, the Young's moduli of intact shale and pertinent softening-induced alterations are evaluated by a novel, large volume (LV)-based statistical nanoindentation technique. This technique is capable of providing a viable, powerful, and repeatable tool to accurately characterize the shale softening behavior as a bulk composite as well as the softening-induced changes in the mechanical properties of individual phases at the micro- to nano-meter scales along the entire softened zone. It can also be implemented as part of a design and optimization protocol for screening various stimulants and additives used in hydraulic fracturing and oil/gas production operations.

2 Materials and Methods

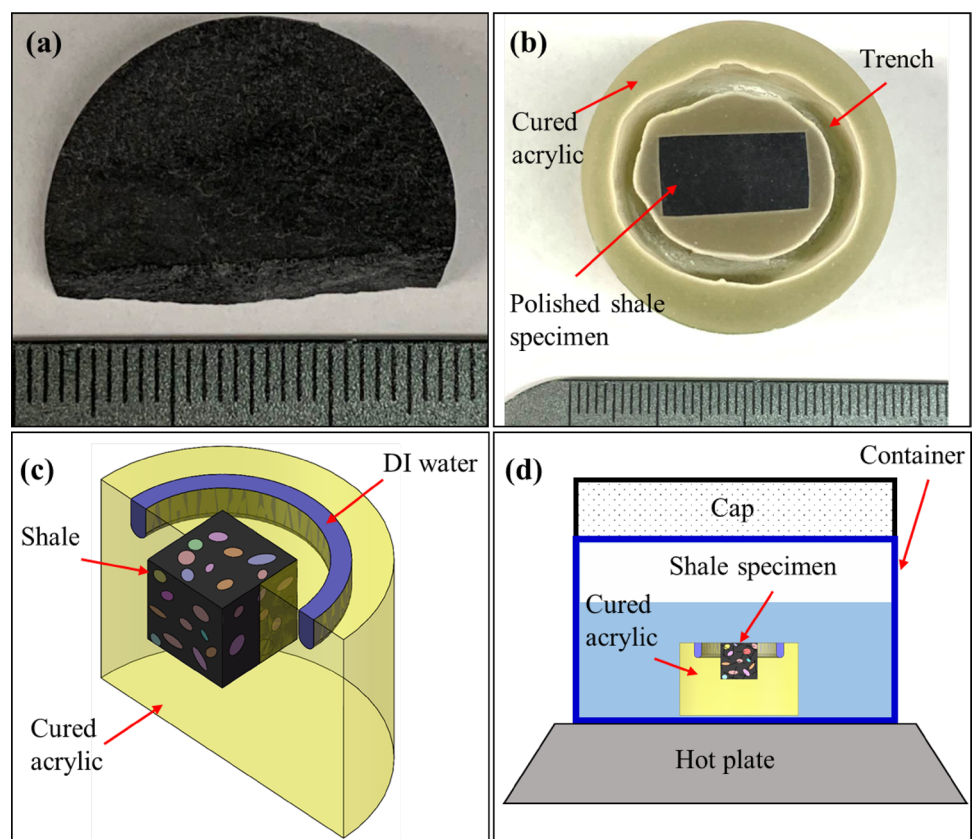
2.1 Samples and Sample Preparation

The studied shale samples were recovered in a horizontal well of 2300–2500 m in depth from the Longmaxi Formation,

Sichuan Basin, China. Cylindrical intact rock cores were used initially for macroscopic triaxial testing, and the fractured triaxial specimens were then used in this study. These fragments were further divided into two groups: while relatively smaller chips were used for mineralogical analysis, the larger blocks with known orientation of the bedding planes were carefully selected for mechanical testing (Fig. 1a).

To prepare samples for nanoindentation testing, a carefully selected shale fragment was cut by a carbide-tipped saw blade into a cuboid with dimensions of $\sim 15 \times 15 \times 13$ mm, followed by embedding into a fast-setting acrylic (Buehler Inc., Illinois, USA) to facilitate subsequent surface polishing and to ensure that water flows or permeates into the specimen only from the polished surface along the vertical direction, but not from the four sides or bottom surface (Fig. 1b, c). A circular trench encompassing the cuboid was created by pre-embedding a strand of sacrificial modeling clay that was subsequently removed upon complete curing of the acrylic, leaving an empty groove surrounding the specimen. During the embedment process, special caution was taken to ensure enough space between the specimen and modeling clay strand used to form the trench when pouring the liquid acrylic (Fig. 1c). In addition, an open-ended plastic tube attached to the indenter tip house was also used to loosely enclose the tested sample disk. During actual measurements, the trench was filled with deionized (DI) water and then

Fig. 1 Sample preparation for nanoindentation and softening treatment: **a** fractured triaxial specimen fragment; **b** Polished shale specimen embedded in acrylic with a trench; **c** three-dimensional perspective of the specimen and embedding acrylic with a trench filled with water; **d** hydrothermal treatment of shale in water at 95 °C for 30 days



the plastic tube was lowered to enclose the sample disk. As such, a ~100% relative humidity was maintained inside the tube, and drying of the wet shale specimen was prevented or minimized during the entire measurement.

The specimen surface parallel to the depositional bedding plane was chosen to accept indentation loading. To minimize the effect of surface roughness on result accuracy (Miller et al. 2008), the exposed surface was first polished successively in a MetaServ 250 polishing machine (Buehler Inc., Illinois, USA) using sandpapers of different grain finenesses from P180 to P4000, and the final polishing used extra fine alumina suspension consisting of 0.3 μm alumina powder and a mixture of ethanol and ethylene glycol at a 1:1 volumetric ratio. At the end of each polishing step, the sample surface was rinsed with ethanol, but not water, to avoid the potential hydration of clay minerals within the shale. As a result, a highly smooth and flat surface with minimized hydration or wetting of clay minerals was prepared for subsequent nanoindentation testing. In a parallel study, the same polishing procedures were used to prepare another shale sample from the same rock formation, and the root-mean-square (RMS) roughness R_q is 138 nm, as characterized by atomic force microscopy.

2.2 X-ray Powder Diffraction

X-ray diffraction (XRD) was employed to determine the mineralogical composition of the shale sample. Small rock chips were first crushed in a percussion mortar and then wet ground in a McCrone Micronizing Mill (The McCrone Group, Westmont, IL) for 15 min to pulverize the sample into a powdery slurry with particle sizes of $<4\ \mu\text{m}$ (Locock et al. 2012). Propan-2-ol (i.e., $\text{C}_3\text{H}_7\text{OH}$) was used as the grinding liquid to minimize the grinding-induced damage to crystal structure, particularly clay minerals, in the shale. The powder slurry was then oven dried at 105–110 $^\circ\text{C}$ for 24 h before XRD characterization.

Another purpose of the XRD analysis was to examine whether the polishing process would cause undesired chemical reactions or change in the mineralogical composition and hence the mechanical properties of the shale. In fact, ethylene glycol [$(\text{CH}_2\text{OH})_2$], an organic compound widely used to expand the d -spacings of smectite or other swelling clay minerals (Moore and Reynolds 1997), may induce the swelling of expandable clay minerals (if any is present) that may further influence the mechanical properties of the bulk rock. Such interactions would negatively affect the nanoindentation results. Therefore, part of the aforementioned powder was further inundated in the ethanol–ethylene glycol (at a 1:1 volumetric ratio) mixture for 24 h, followed by oven drying prior to XRD characterization.

For quantitative analysis, 10 wt % zincite (ZnO), used as an internal standard, was thoroughly mixed into the dried

powder. To achieve better random orientation of platy clay minerals, the razor-tamped surface (RTS) method (Zhang et al. 2003) was adopted to prepare the powder mount on the sample holder. All diffraction patterns were obtained in a PANalytical X'Pert PRO X-ray diffractometer (Almelo, Netherlands) equipped with a Ni filter, using Cu-K α radiation ($\lambda = 1.5418\ \text{\AA}$) generated at 45 kV and 40 mA, a continuous scan range of 2° – $64^\circ\ 2\theta$, and a scan speed of $1^\circ\ 2\theta/\text{min}$. Profex, an open-source program with the Rietveld refinement method (Doebelin and Kleeberg 2015), was used to perform both qualitative and quantitative analyses of the acquired XRD patterns.

2.3 Nanoindentation Testing

Nanoindentation typically involves pushing a small and sharp indenter made of very hard materials (e.g., usually diamond) into a softer sample during which the load (F) and depth (h) are recorded (Fig. 2). The F – h curves are then analyzed to extract the mechanical properties of the tested material by, for example, the Oliver and Pharr method (Oliver and Pharr 1992). The contact stiffness S is defined as the slope of the initial unloading curve at the maximum depth h_{max} :

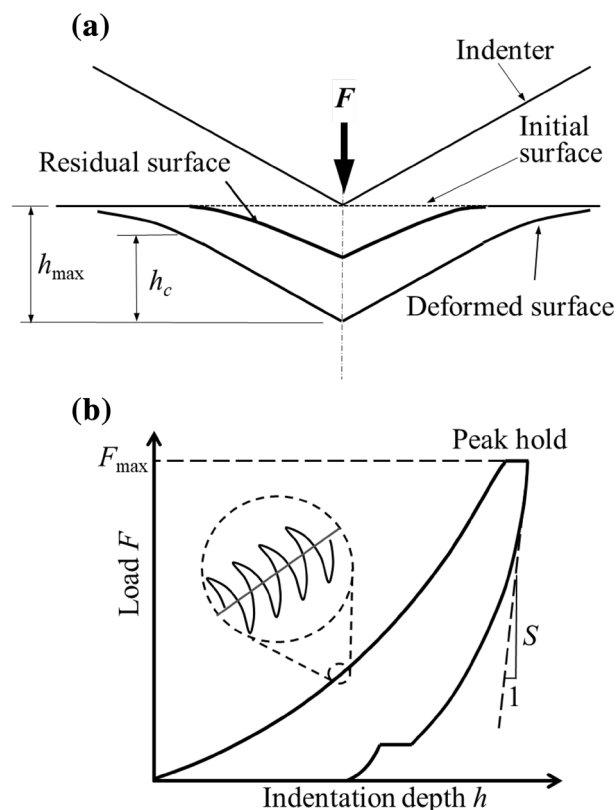


Fig. 2 Schematic of nanoindentation testing: **a** penetration of indenter into the sample; **b** the recorded load–displacement curve showing the loading/unloading cycle under the CSM mode

$$S = \frac{dF}{dh} \Big|_{h = h_{\max}} \tag{1}$$

The reduced modulus E_r is then determined based on the contact stiffness via the following equation:

$$E_r = \frac{\sqrt{\pi}}{2\beta\sqrt{A_c}} S, \tag{2}$$

where β is a dimensionless correction factor for indenter geometry and $\beta=1.05$ is commonly adopted for a Berkovich indenter, A_c is the projected contact area, which can be calculated from the calibrated tip function, defined as:

$$A_c = C_0 h_c^2 + \sum_{j=1}^8 C_j h_c^{\left(\frac{1}{2}\right)^{j-1}} \tag{3}$$

where C_j ($j=0, 1, 2, 8$) are constants calibrated with the results of standard materials (e.g., fused silica, aluminum) with known mechanical properties; h_c , the contact depth, can be determined by the Oliver and Pharr method (Oliver and Pharr 1992, 2004),

$$h_c = h_{\max} - h_s = h_{\max} - \varepsilon \frac{F_{\max}}{S} \tag{4}$$

where h_s is the purely elastic deflection of the sample surface at the contact perimeter, F_{\max} is the maximum load, and ε is a geometric constant for the indenter (for a Berkovich tip, $\varepsilon=0.75$). To account for the elastic deformation occurring in both a non-rigid indenter and the sample, the Young’s modulus of the sample can be extracted by the following relationship (Johnson 1985; Doerner and Nix 1986):

$$\frac{1}{E_r} = \frac{1 - \nu^2}{E} + \frac{1 - \nu_i^2}{E_i} \tag{5}$$

where E and ν are the Young’s modulus and Poisson’s ratio of the sample, and E_i and ν_i are the same parameters of the indenter, respectively. For a diamond indenter, E_i and ν_i are 1141 GPa and 0.07, respectively. The Poisson’s ratio is squared in the above equation and hence its variation has little effect on the calculated sample modulus E (Menčík et al. 1997; Mesarovic and Fleck 1999; Saha and Nix 2002). A constant Poisson’s ratio of 0.2 was assumed for both the intact and hydrated shale samples.

All nanoindentation tests were conducted in a Keysight G200 nanoindenter (Keysight Technologies, Inc., Santa Rosa, CA) equipped with a Berkovich diamond indenter with a tip radius of <20 nm. Indentation loading employed a continuous stiffness measurement (CSM) method, which imposed a small displacement-controlled harmonic oscillation with a frequency of 45 Hz and an amplitude of 2.0 nm on the primary monotonic loading signal and allowed the

harmonic contact stiffness to be continuously determined. Hence, based on Eqs. (1–5), the Young’s modulus of the tested material was determined as a function of indentation depth. In addition, all indentation tests were run with an allowed thermal drift rate of <0.05 nm/s, a constant indentation strain rate \dot{h}/h of 0.05 s⁻¹ to a maximum load of 620 mN, which resulted in maximum indentation depths of 3000–6000 nm depending upon the indented locations (e.g., relative hard quartz particles vs. relatively soft clay matrix), and a 60-s holding time at the maximum load prior to unloading.

A total of 21 matrices of indents, each of which consisted of a 7 × 7 grid with a spacing of 200 μm, were conducted on different, randomly selected zones of the polished sample surface, resulting in a total of 1029 indentation measurements on each surface. Such a large number of total indents and matrices is expected to overcome the potential unknown surface heterogeneity, as pointed out by others (e.g., Zhu et al. 2007). More importantly, another major reason for choosing a 7 × 7 grid is to maintain high efficiency and data quality, via a rigorous scheme for tip cleanliness and tip calibration. Upon the completion of each matrix, the tip was cleaned and recalibrated on the standard fused silica to verify the tip surface was clean or free of potential damage. If unexpected results on the fused silica were obtained, then the results from the previous matrix of indents were discarded, and the tip was recleaned and recalibrated before continuing to the next matrix. As such, if a relatively large matrix was scheduled and the tip was contaminated in one but unknown indent, then all of the results from this large matrix could not be used and part of the sample was consumed or wasted.

After indentation unloading, all residual indents were carefully examined and imaged with the built-in optical microscope with either a 10X or 40X objective. Before statistical analysis, pre-screening of the $F-h$ curves combined with the careful examination of the corresponding residual indent images (e.g., indent geometry, coincidence of indentation points with pores or voids) was conducted to remove and discard these obvious outliers, ensuring that all data included in the statistical analysis had certain reliability.

2.4 Large Volume (LV)-Based Nanoindentation

In this study, a novel technique, LV-based statistical nanoindentation, was developed for the first time to study the shale softening behavior, including the rate of softening advancement, and to further uncover the physico-chemical mechanisms controlling the softening phenomenon. After indentation measurements were conducted on the untreated (or non-hydrated) sample surface to obtain the baseline reference data, the indented layer with a thickness much

greater than the depth of the residual indents was removed via polishing. The polished sample was then inundated for 30 days in DI water at an elevated temperature of 95 °C to simulate the deep underground hydrothermal environment encountered in hydraulic fracturing and subsequent oil/gas extraction processes (Fig. 1d).

Such a treated sample was then further probed by the so-called LV-based indentation, which consisted of two steps (Fig. 3): (1) the same grid indentation technique described above was used to collect meaningful data from the polished surface (denoted as polished depth $d=0$) by performing a massive number (i.e., $7 \times 7 \times 21 = 1029$) of indents at randomly selected locations; (2) the indented surface layer with a thickness much greater than the depth of residual indents was sacrificially removed by further polishing, to eliminate the elasto-plastic zone induced by prior indentation loading. These steps were sequentially repeated by alternating indentation and polishing with the sacrificial layer-by-layer removal of the pre-indented surface layer. As such, interested data at different, carefully measured polished depths (i.e., $d=0, 15.0, 142.5, 314.0 \mu\text{m}$) beneath the original surface were obtained. The experiment was stopped when the results from a freshly polished surface at depth were approximately the same as the baseline reference data from the untreated surface. With this technique, the Young's moduli of mechanically distinct phases can be statistically extracted from the massive datasets obtained from a series of polished depths (i.e., $d=0$ to $314.0 \mu\text{m}$ or a large volume). Moreover, the subtle changes in the mechanical properties of different phases at different depths can be quantitatively analyzed to characterize the shale softening behavior.

2.5 Statistical Deconvolution

Statistical deconvolution of the massive indentation data was performed based on their cumulative distribution function (CDF) (Ulm et al. 2007). Its advantage over the probability density function (PDF)-based method is that the former eliminates the need for selecting an appropriate bin size required for generating the PDF plots required in subsequent statistical analysis. For a random variable (x) with a normal distribution, the cumulative distribution function is given by:

$$F(x|\mu, \sigma) = \frac{1}{\sigma\sqrt{2\pi}} \int_{-\infty}^x e^{-\frac{(t-\mu)^2}{2\sigma^2}} dt \quad (6)$$

where μ is the mean value, and σ is the standard deviation.

For a multiphase composite, the experimentally obtained Young's modulus of each phase is a random variate, assumed to follow the Gaussian distribution. The cumulative distribution function, $g_{\text{data}}(x)$, of all experimental data obtained from the composite can be fitted by the following function:

$$g_{\text{data}}(x) = a_1 F(x|\mu_1, \sigma_1) + a_2 F(x|\mu_2, \sigma_2) + \dots + a_n F(x|\mu_n, \sigma_n) \quad (7)$$

$$\sum_{i=1}^n a_i = 1 \quad (8)$$

where n is the number of phases in the composite, which can be determined by XRD, and a_i is the volumetric fraction of each individual phase. Then, the least squares method is

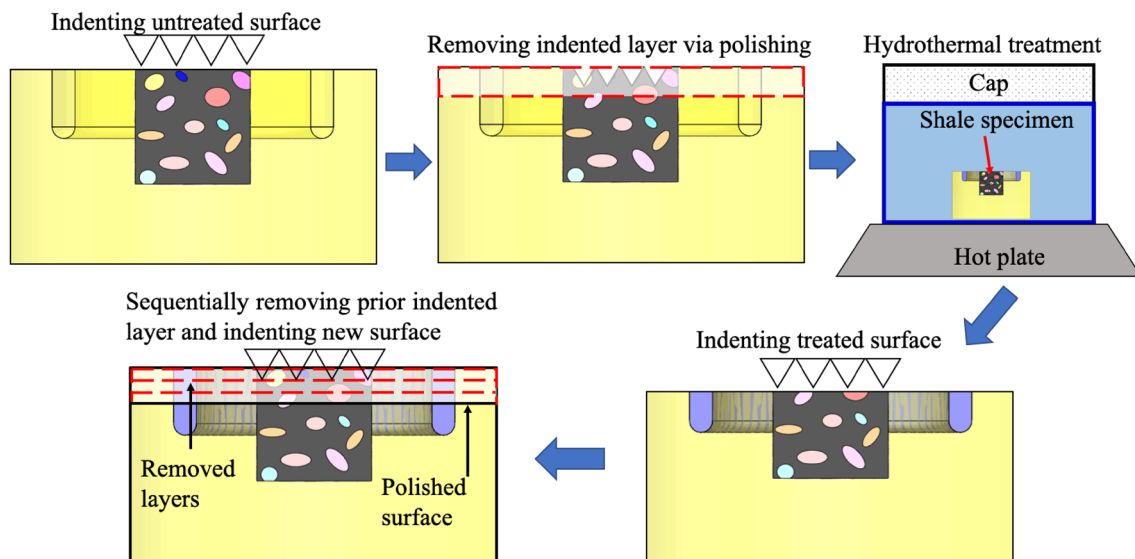


Fig. 3 Schematic of the large volume-based indentation technique: alternately indenting the hydrothermally treated surface and removing prior indented layer via polishing

used to find the optimal values of μ_i, σ_i, a_i , where $i = 1, 2, 3, \dots, n$, from

$$\min \frac{1}{n} \sum_{i=1}^n [g_{\text{data}}(x_i) - g(x_i)]^2 \tag{9}$$

To avoid the excessive overlap of the neighboring Gaussian variates, the deconvolution results were further constrained by DeJong and Ulm (DeJong and Ulm 2007):

$$\mu_i + \sigma_i \leq \mu_{i+1} + \sigma_{i+1} \tag{10}$$

For each mineral phase, initial values, μ_{i0} and σ_{i0} , required as input for deconvolution were derived from the published data (as described later in Table 2). Results derived from the statistical deconvolution include the volumetric fraction a_i , mean μ_i , and standard deviation σ_i of all mechanically distinct phases.

Since the CSM method provided the continuous measurements of Young’s modulus over the entire indentation depth (e.g., up to ~6000 nm), a novel statistical deconvolution technique was first used in this study: the continuous $E-h$ curves were fragmented at different indentation depths with intervals of 250 and 500 nm for $h < 2500$ nm and $h = 2500-6000$ nm, respectively (Fig. 4). This fragmentation resulted in a total of 17 data subsets, each of which contained ~1029 dependent measurements at a fixed depth. Each of the 17 data subsets on the Young’s modulus at a fixed indentation depth was then used to construct the depth-dependent CDF plot that was then deconvoluted by the aforementioned method. As such, depth-dependent Young’s moduli of different mineral phases were obtained, and the dependence of the Young’s modulus upon indentation depth was further fitted by a newly proposed “surround effect” model, as described below. Moreover, this entire process was repeated for each of the four freshly polished surfaces (i.e., at 4 polished depths, $d = 0, 15.0, 142.5, 314.0 \mu\text{m}$). In summary, massive data from five freshly polished surfaces (including one untreated surface and four polished surfaces on the softened sample), each with ~1029 indents to indentation

depth of up to 6000 nm that were fragmented into 17 data subsets, were analyzed, resulting in 85 CDF-based deconvolutions, each with ~1029 data entries.

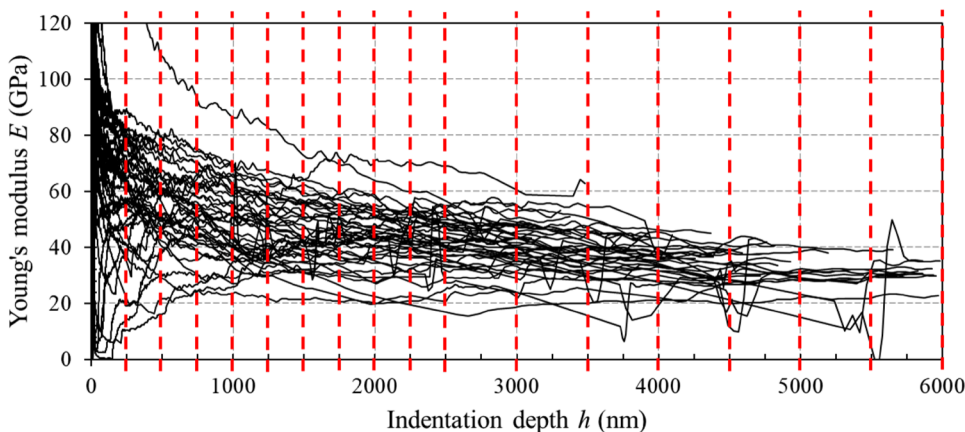
2.6 Surround Effect Model

The substrate effect has been observed on the nanoindentation data obtained from thin films (Tsui and Pharr 1999; Saha and Nix 2002), and much effort was taken to characterize and analyze the mechanical properties of thin films by eliminating the substrate effect. For instance, a common rule of thumb for measuring the film-only properties is that the indentation depth should be limited to <10% of the film thickness. Both finite element analysis (e.g., Fischer-Cripps 2007) and nanoindentation experiments (e.g., Saha and Nix 2002) have been conducted to study the effects of the substrate on the determination of mechanical properties of thin films. In fact, at large indentation depths, the elastic zone beneath the indenter tip is not constrained only within the film, but rather expands to the substrate.

Although the analogy between the thin film–substrate system and heterogeneous multiphase shale was previously recognized (e.g., Constantinides et al. 2006), this phenomenon has not been modeled explicitly, but rather used for the selection and optimization of an appropriate indentation depth for testing heterogeneous materials (e.g., shale, concrete). In this paper, a newly proposed “surround effect” model, similar to the substrate effect model proposed by Wei et al. (Wei et al. 2009), was used to analyze the depth-dependent variations of the Young’s modulus of each individual phase, excluding the interface between two mechanically contrasting phases (as described in Sect. 3.4 in details):

$$E = E_c + \frac{E_p - E_c}{1 + [h/(t\beta)]^Y} \tag{11}$$

Fig. 4 Segmentation of the $E-h$ curves from one 7×7 matrix of indents at different indentation depths



where t is the characteristic length scale of the individual phases; Y and β are two constants that can be determined through the model fitting; E_p and E_c are the predicted Young's moduli of the individual phases and the bulk rock, respectively; E is the varying Young's modulus at a specific indentation depth. The deconvoluted data from Sect. 2.6 obtained on each of the five polished surfaces were then fitted by this surround effect model using a statistical analysis program SAS (SAS Institute, Inc., North Carolina, USA), leading to the determination of E_p and E_c , the Young's moduli of individual phases and the bulk rock, respectively.

3 Results and Discussion

3.1 Mineralogical Composition

Figure 5 compares the diffraction patterns of the wet ground powder samples with and without prior ethanol–ethylene glycol treatment. As shown in the figure, the two patterns are visually identical, and no shift in the diffraction reflections takes place, indicating that the polishing liquid consisting of ethanol and ethylene glycol causes no changes in the $d(001)$ spacings of clay minerals or in the mineralogical composition. If the shale contained expandable clay minerals such as smectite or vermiculite, the swelling of these expandable minerals caused by the solvation of ethylene glycol into the interlayer space would alter their mechanical properties and hence the bulk shale. As such, comparison of the diffraction patterns further validate that the adopted water-free polishing method has no discernible effects on the sample's mineralogical composition.

Table 1 summarizes the mineralogical composition of the shale obtained from quantitative XRD analyses. Relatively hard minerals, including quartz and albite (a plagioclase feldspar), are the major phases that make up 68.8 wt % of the bulk rock. Due to the high fractions of

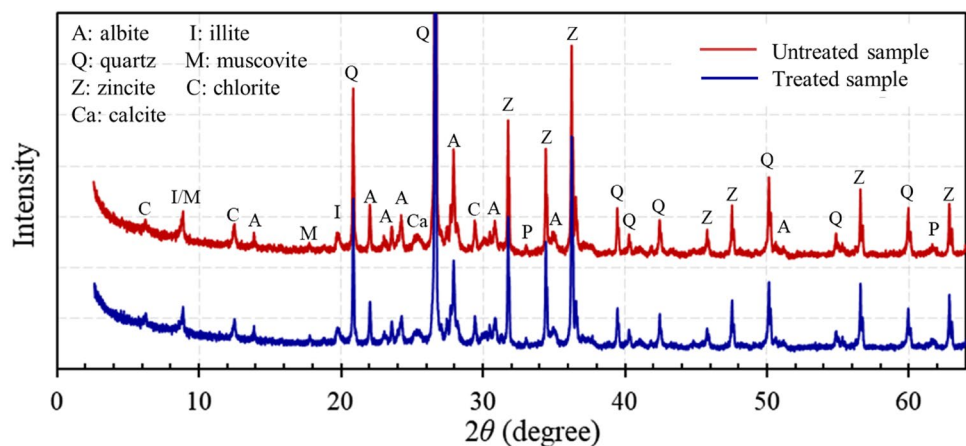
Table 1 Composition of the studied shale sample

Mineral name	Fraction (wt %)	Specific gravity	Volumetric fraction (vol. %)
Chlorite	5.2	2.6	5.3
Illite	10.0	2.6–3.3	8.9
Muscovite	12.0	2.8–3.0	10.9
Quartz	43.4	2.6	43.8
Albite	23.4	2.6	23.6
Calcite	2.3	2.7	2.2
Pyrite	2.0	5.0–5.1	1.3
Organic matter ^a	1.7	1.06	4.0

^aFrom Huang et al. (2015)

hard minerals, especially quartz at a fraction of 43.4 wt %, it can be inferred that the shale is expectedly relatively brittle with a high elastic modulus and hardness and can be easily fractured to create extensive fracture networks (Rickman et al. 2008; King 2010). Clay minerals, including chlorite, illite, and muscovite, widely found in shales, are also present in this sample, and their total fraction is 27.2 wt %. On the other hand, calcite, which are considered as cementing or bonding materials that fill the natural pores and cracks in shale formations, are a minor phase with a fraction of 2.3 wt %. Also, a small amount of pyrite (2.0 wt %), a common mineral found in shales, is also present. Due to the non-crystalline nature of organic matter (e.g., typically kerogen), the amorphous phase with a percentage of 1.7 wt % is assigned to the organic matter. Also shown in this table are the volumetric fractions of these minerals, which are estimated based on their mass fractions and specific gravities, with the latter found in the literature (Speight 2005). The volumetric fractions obtained by XRD will be subsequently used to determine the number of mineral phases used in statistical deconvolution.

Fig. 5 XRD patterns of the studied shale sample with and without treatment in polishing liquid



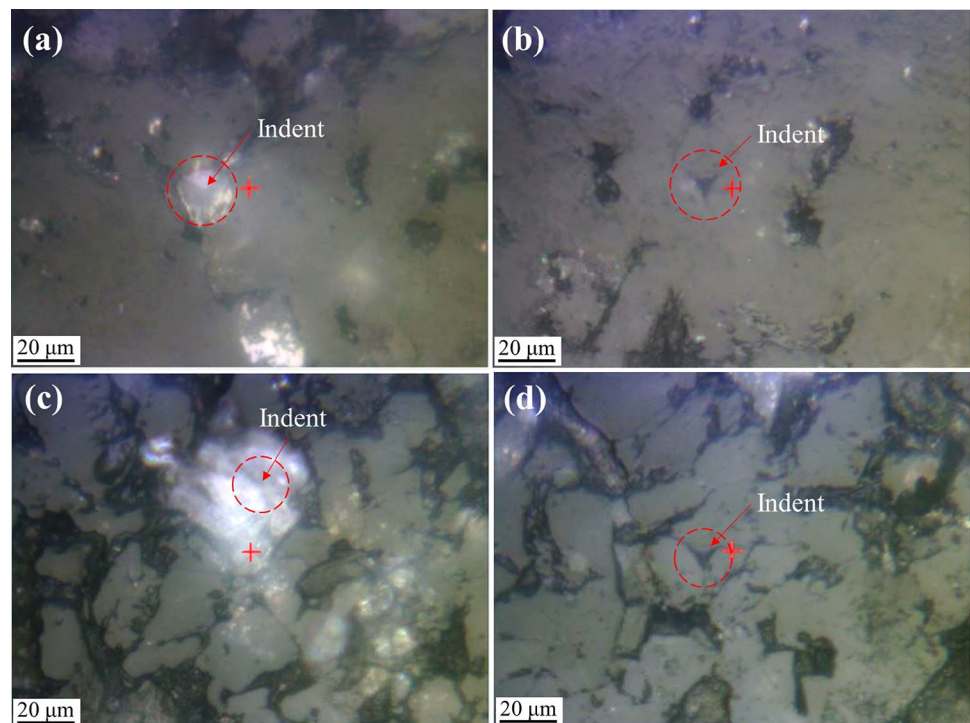
3.2 Nanoindentation Behavior

Figure 6 shows some typical residual indents on the untreated and hydrothermally treated sample surfaces: while two are located at the interface between hard solid particles and clay matrix (Fig. 6a, c), the other two are made on quartz particles (Fig. 6b, d), which can also be verified by the corresponding indentation load–depth curves. For example, since quartz is a very hard and stiff mineral, the size or depth of the residual indents made on a quartz particle is much smaller than that on clay matrix or other softer phases (e.g., organic matter). Again, the use of the CSM method ensures that the Young's modulus of the shale sample over the entire indentation depth is acquired continuously.

As mentioned earlier, a total of 21 matrices of indents were performed on each polished surface, and it would be infeasible to show all of these curves. As examples, Fig. 7 shows some typical results of the $F-h$ curves from the untreated and hydrothermally treated surfaces as well as the corresponding Young's modulus. Obviously, the $F-h$ curves are typical of rocks, and those in Fig. 7a obtained from the untreated surface are in general much stiffer than those in Fig. 7b from the hydrothermally treated surface. Moreover, almost all the $E-h$ curves show a depth-dependent Young's modulus with relatively larger variations at shallow depths and then gradually converge with increasing depth (Fig. 7c, d). Some curves start with a smaller Young's modulus at shallow depths, which then gradually increases with depth, while others show the opposite

trend. Although the preset maximum indentation depth is 6000 nm, most of the $E-h$ curves from the untreated surface (Fig. 7a) end at $h \sim 4000-5000$ nm due to the limitation of maximum load capacity (i.e., set to 625 mN), which also affects the maximum achievable indentation depth (e.g., if the indent is made on a relatively hard particle such as quartz, then the maximum achievable indentation depth is smaller). In contrast, for the hydrothermally treated surface (Fig. 7b), most $E-h$ curves reach the preset maximum depth of 6000 nm, indicating that the hydrothermal treatment even at ambient pressure can soften the shale, particularly at the shallow surface layer. Such softening can also be verified by a simple comparison of the arithmetically averaged E values for all 49 indents at a relatively large indentation depth (e.g., $h = 3000$ nm): the untreated surface has an average E of 50.8 GPa, while the treated surface has an average E of 29.2 GPa, a 42.5% reduction caused by the hydrothermal treatment. In fact, as discussed later, the Young's moduli at larger indentation depths can be used to approximate the bulk property, and the reduction in the Young's modulus of the bulk rock is a clear indicator of softening. In summary, the two sets of $E-h$ curves in Fig. 7 demonstrate the representative features of the mechanical response over the entire indentation depth for all other indentation measurements, and it can be concluded that the shale's Young's modulus is obviously altered by prolonged hydrothermal treatment (i.e., 30 days inundation in water at 95 °C).

Fig. 6 Selected optical images of polished sample surfaces showing residual indents at: **a** pyrite–quartz interface; **b** a quartz particle; **c** pyrite–quartz interface; **d** a quartz particle. **a** and **b** untreated sample surface; **c** and **d** treated sample surface



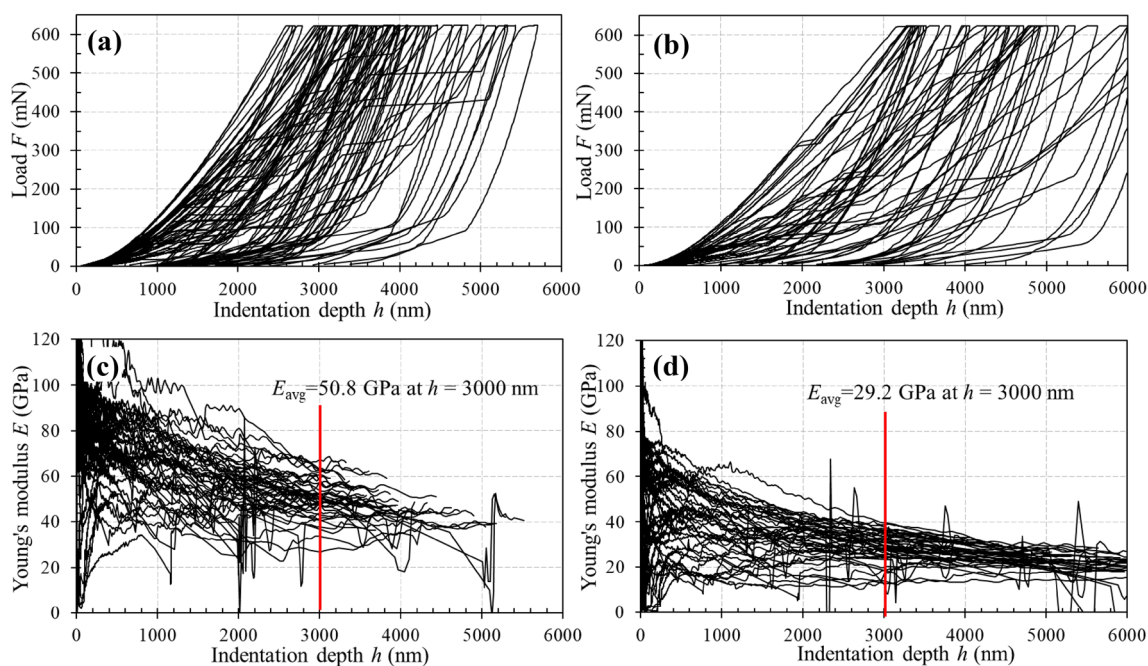


Fig. 7 Typical CSM indentation results from a 7×7 matrix of indents showing the dependence of Young's modulus on indentation depth: **a** F – h curves for the untreated surface; **b** F – h curves for the

hydrothermally treated surface; **c** E – h curves corresponding to (a); **d** E – h curves corresponding to (b)

3.3 Statistical Deconvolution

The CDF-based deconvolution requires the number of total phases in the rock as an input parameter. Based on the XRD analysis (Table 1), the shale contains eight different minerals in total. However, since the platy clay particles are very small, usually with a typical planar dimension of $< 2 \mu\text{m}$ and a thickness of $< 0.2 \mu\text{m}$ (i.e., the thickness is 1/10 of the planar dimension or even smaller), it is impossible to detect and discern the independent mechanical response of individual clay particles even at indentation depth as small as $h = 250 \text{ nm}$, which may induce an elastic zone of $10 \times h = 2.5 \mu\text{m}$ in size. Such an elastic zone size well exceeds the clay particle thickness (i.e., $0.2 \mu\text{m}$). Moreover, as a sedimentary rock, secondary interparticle and pore-filling cementation such as calcite exists throughout the entire rock, and the cementation minerals may be very tiny owing to the size constraints of initial pores (i.e., voids prior to the precipitation of cementation minerals). As such, all clay minerals together with the interparticle cementation minerals (e.g., calcite) are treated as a homogenized clay matrix. Finally, pyrite usually exists as spherical framboids consisting of numerous nano-sized crystals and intra-framboid voids, and the studied shale only contains 1.3 vol. % pyrite. Statistical nanoindentation may not be able to detect pyrite separately due to either its too low volumetric fraction or its too small particle size. Therefore, pyrite is also included in the clay matrix.

In summary, the clay matrix consists of two clay minerals (i.e., chlorite and illite), a cementation mineral (i.e., calcite), and a low-fraction and small-sized mineral (i.e., pyrite). From Table 1, the sample contains other four phases, muscovite, quartz, albite, and organic matter, at a significant volumetric fraction, which are expected to be discernable by nanoindentation. Finally, those indents with a finite, but not infinitesimal depth may coincidentally be located at the interfaces of different minerals, particularly hard minerals such as quartz and the relatively softer clay matrix. Then, the mechanical response to indentation loading is determined by the indenter-induced elasto-plastic zone encompassing both hard and soft minerals. With increasing indentation depth, such a virtual phase is easier to detect and becomes more pronounced. In conclusion, a total of six mechanically distinct yet indentation-discernible mineral phases are used for the CDF-based deconvolution.

As an example, Fig. 8a shows typical CDF-based deconvolution results from ~ 1029 indents at depth of $h = 250 \text{ nm}$, made on the untreated sample. The six mechanically distinct phases are, respectively, assigned as organic matter or kerogen as pore-filling material, clay matrix, interface between hard and soft phases (e.g., clay matrix–quartz interface), albite, muscovite, and quartz in the order of increasing Young's modulus. Figure 8b shows the corresponding, visually more intuitive PDF curves obtained by taking the first-order derivative of the CDF curves. Based on

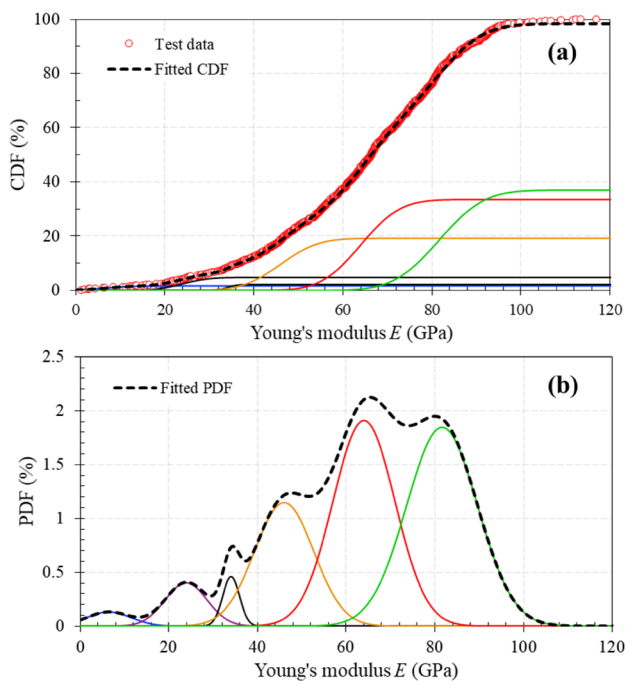


Fig. 8 Example results of deconvolution of Young’s modulus: **a** overall CDF and the deconvoluted CDF for individual phases; **b** PDF derived by taking the first-order derivative of CDF

the deconvoluted CDF or PDF curves, the statistical mean and standard deviation of each phase’s Young’s modulus are obtained.

For the untreated sample surface, similar deconvolutions are performed at other selected indentation depths (e.g., $h = 250, 500, 750, \dots, 2500, 3000, \dots, 6000$ nm; Fig. 4). Such a series of analyses yields a dataset linking the Young’s modulus of each individual mineral with indentation depth, which are plotted in Fig. 9a. Clearly, these data points stay apart at shallow indentation depths, and then gradually converge with increasing depth. Such a relationship between the Young’s modulus of individual phases and indentation depth is fitted by the surround effect model, and the results are shown in Fig. 9b where the indentation depth is plotted at a logarithmic scale to show clearly the trend at smaller depths and to ease the data fitting of the surround effect model.

The five fitting curves of the surround effect model for the five mineral phases (i.e., excluding the interface as a virtual phase) show some interesting features:

- The Young’s modulus of relatively hard minerals (e.g., quartz) gradually decreases with depth, while that of soft phases (e.g., clay matrix) shows the opposite trend;
- All five fitting curves converge to a nearly constant value or a narrow band, ~ 45 GPa, at larger depths (e.g., $h > 10$ μm), which is regarded as the Young’s modulus of the bulk rock (i.e., as a composite), because the relatively

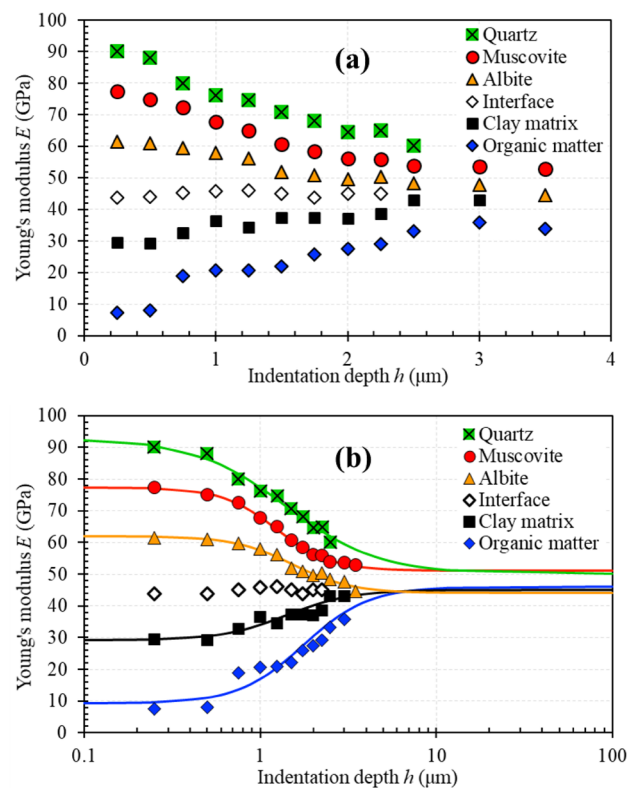


Fig. 9 The dependence of Young’s moduli of individual phases on indentation depth: **a** deconvoluted results plotted at the linear scale; **b** curve fitting with the surround effect model

large elasto-plastic zone beneath the indenter tip may encompass all major minerals that act together as a composite to resist the indentation loading. Similar observations and conclusions were made by others (e.g., Bennett et al. 2015);

- The Young’s moduli of these fitting curves at very small indentation depth (e.g., $h = 0.1$ μm) are the in situ moduli of individual mineral phases, which are usually difficult to obtain due to the surface roughness and surface contamination. However, statistical indentation makes it possible to determine the in situ mechanical properties of individual mineral phases virtually at an infinitesimal depth;
- Particularly noteworthy is the Young’s modulus of a virtual phase, the interface between the soft and hard minerals, which has little variation over the entire indentation depth and is just slightly less than that of the bulk rock. As such, it might be feasible and practically attractive to conduct indentation measurements particularly on the interfaces of hard and soft minerals, and then use the interface’s Young’s modulus to approximate the bulk rock’s elasticity.
- The Young’s moduli of individual phases are derived from the fitted surround effect model at a theoretical

indentation depth $h=0$, and results are shown in Table 2, which are in excellent accordance with the Young's moduli of these minerals found in the literature. For example, the Young's modulus of organic matter is consistent with those found in the literature (e.g., (Eliyahu et al. 2015; Ahmadov et al. 2009). In fact, such a good agreement can also validate the accuracy of the results as well as the pertinent CDF-based deconvolution method.

3.4 Characterization of Softening Behavior

Results presented in the prior section yield the baseline elastic properties of the untreated sample. The changes in the

Table 2 Summary of the Young's moduli of individual minerals determined by statistical deconvolution

Mineral	This study (GPa)	Reported value (GPa)
Quartz	92.2	87.2–105.8 [37]
Muscovite	77.5	79.3 ± 6.9 [38]
Albite	62.0	62.0 ± 6.0 [39]
Clay matrix	29.2	26.0 ± 5.7 [22]
Organic matter	9.3	0.0–25.0 [40]

Young's modulus of the hydrothermally treated or softened sample were investigated by the LV-based statistical indentation, which are shown in Fig. 10. The deconvoluted Young's moduli of different mineral phases at varying indentation depths h as well as four different polished depths d (i.e., different from h) are compared and are fitted by the surround effect model in this figure. In general, the polished depths are much greater than the indentation depths.

A simple comparison between Figs. 9b and 10a indicates that the Young's moduli of all minerals at the softened surface (i.e., at the polished depth $d=0$) are significantly smaller than those of correspondingly respective phases in the untreated sample (i.e., the baseline data). For example, the Young's moduli of quartz, muscovite, and albite are all reduced, despite their chemically relatively stable nature. In fact, prior work also showed that the Young's moduli of all soft and hard minerals in different shale formations decreased after exposure to the 2 wt % KCl slick water fracturing fluids (Akrad et al. 2011). This phenomenon is attributed to the significant softening (i.e., the decrease in Young's modulus from 29.2 to 16.5 GPa) of the clay matrix that acts as a foundation supporting and enclosing those hard minerals. If the particle sizes of these hard minerals are not sufficiently large, the indentation-induced elastic zone can

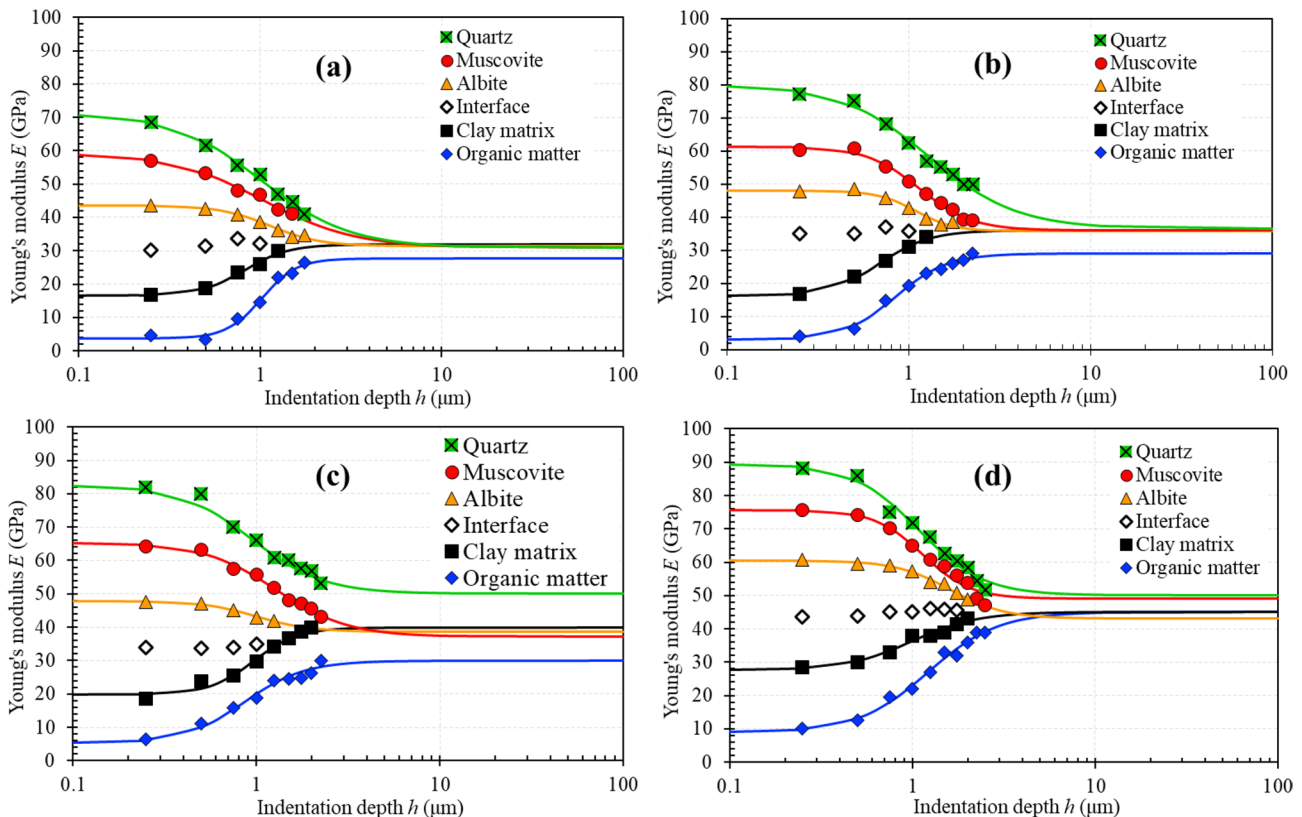


Fig. 10 Deconvoluted results and fitting curves of the surround effect model at different polished depths: **a** $d=0$, the initial water–rock contact surface; **b** $d=15 \mu\text{m}$; **c** $d=142.5 \mu\text{m}$; **d** $d=314 \mu\text{m}$

expand beyond these particles into the softened clay matrix. As such, the softening and weakening of the clay matrix can cause whole hard mineral particles to sink into the clay matrix under indentation loading (Leisen et al. 2012). In general, this is also the so-called “surround effect”. Practically, upon prolonged exposure of the fractured surfaces to fluids, especially in a hydrothermal environment, proppants together with the hard minerals may easily embed into the softened clay matrix.

Particularly noteworthy is the reduction (i.e., from 9.3 to 3.8 GPa) in the Young’s modulus of a soft phase, organic matter (i.e., typically kerogen), which usually co-exists with clay minerals in the pores and cracks of shale (Salmon et al. 2000; Kuila et al. 2014) and is commonly considered as hydrophobic materials that rarely react or interact with water (Hu et al. 2016). In view of this, reduction in the Young’s modulus of organic matter can be attributed to the decrease in the mechanical properties of the clay matrix, or interpreted by the “surround effect”.

All fitting curves of the surround effect model for different phases converge at larger indentation depths (e.g., $h > 10 \mu\text{m}$) to a value also significantly smaller than that of the untreated sample. This converged value, regarded as the property of the bulk rock, further demonstrates the softening phenomenon caused by the prolonged hydrothermal treatment. In summary, after hydrothermal treatment, the Young’s moduli of both individual minerals and the bulk shale are significantly reduced.

Similarly, Fig. 10b–d summarize the results for the other three polished depths (i.e., $d = 15.0, 142.5,$ and $314.0 \mu\text{m}$), measured from hydrothermally treated or softened surface. In Fig. 10b, the Young’s modulus of the clay matrix is almost the same as that of the original softened surface (Fig. 9b), suggesting that the clay matrix at this polished depth (i.e., $d = 15.0 \mu\text{m}$ beneath the original surface) is still fully hydrated or completely softened, same as the original surface that is in direct contact with water. In Fig. 10c, the Young’s modulus of the clay matrix is significantly greater than that of the previous two polished depths (i.e., $d = 0$ and $15.0 \mu\text{m}$), indicating that the clay matrix at this polished depth (i.e., $d = 142.5 \mu\text{m}$) is likely just partially hydrated or softened after 30 days’ hydrothermal treatment. In other

words, clay mineral hydration or water–shale interactions may take place at this depth, but not to the maximum extent, since the infiltration or permeation of water into tight formations such as shale takes time. Finally, in Fig. 10d, the Young’s moduli of each mineral are almost the same as the baseline reference data obtained from the untreated sample, indicating that the material at this polished depth has not yet been affected by the softening treatment. The small differences may be caused by experimental errors, sample heterogeneity, and the statistical deconvolution technique.

The Young’s moduli of individual phases obtained from the four polished depths of the hydrothermally treated sample as well as the untreated surface (i.e., the baseline reference) are collectively summarized and plotted in Table 3 and Fig. 11, respectively. It can be seen that the Young’s moduli of all phases decrease significantly, when compared with the baseline data, due to prolonged hydrothermal treatment at elevated temperatures leading to shale softening. For example, the Young’s modulus of clay matrix decreases from 29.2 to 16.5 GPa (i.e., a 43% reduction), while that of the bulk rock decreases from 47.3 to 30.6 GPa (i.e., a 35% reduction). Another striking feature is that the Young’s modulus of each mineral gradually increases with increasing

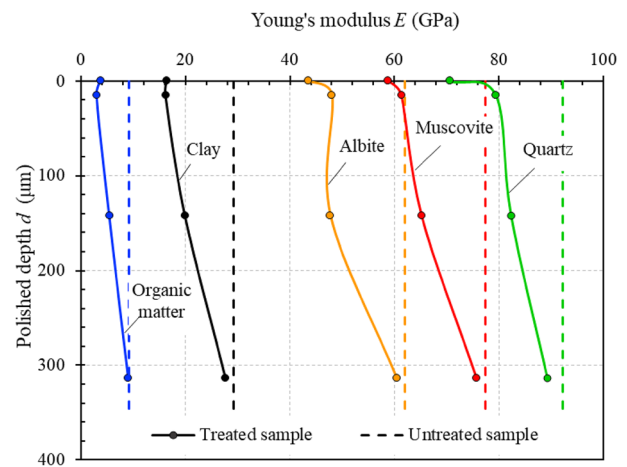


Fig. 11 Changes in the Young’s modulus of individual phases with depth caused by the hydrothermal treatment, showing that the Young’s moduli recover back to the initial baseline values

Table 3 Comparison of the Young’s moduli of different mineral phases and bulk rock at different polished depths after hydrothermal treatment

Polished depth (μm)	Young’s modulus (GPa)					
	Quartz	Muscovite	Albite	Clay matrix	Organic matter	Bulk rock
Untreated surface (baseline data)	92.2	77.5	62.0	29.2	9.3	47.3
0	70.6	58.8	43.5	16.5	3.8	30.6
15.0	79.4	61.3	48.0	16.2	3.0	34.7
142.5	82.2	65.2	47.8	20.0	5.4	41.0
314.0	89.3	75.7	60.5	27.7	9.1	46.4

polished depths, indicating that the degree of softening is not uniform with depth or the softening advancement takes time. In general, the deeper the tested surface, the smaller the reduction in the Young's modulus, or the weaker the hydration of clay minerals. For instance, it is reported in the literature that the degree of softening is significantly influenced by extent of clay minerals swelling (Wong 1998). At the cumulative polished depth of ~314 μm , the corresponding Young's modulus of each individual mineral eventually recovers back to the baseline reference values of the untreated sample. It is then reasonable to postulate that the softening reaction has not advanced to this depth. Therefore, the average rate of softening advancement, defined by the ratio of total thickness of the softened layers to the total treatment time, is estimated as ~10.5 $\mu\text{m}/\text{day}$. Such a value can only be obtained via small-scale measurements, such as the LV-based nanoindentation developed in this study, but not by macroscale measurements such as triaxial element testing.

3.5 Discussion on Softening Mechanisms

Based on the above results obtained from a relatively large volume (or at least a large depth) when compared with conventional nanoindentation testing (e.g., only a few micrometers in depth), the Young's moduli of the bulk shale as well as individual mineral phases significantly decrease after hydrothermal treatment, but such a reduction gradually diminishes at large depths inside the rock. Multiple factors may induce shale softening, including (but not limited to) clay mineral hydration and swelling, dissolution of certain solid phases (e.g., carbonates), unloading-induced rebounding/swelling, and oxidation of certain minerals (e.g., pyrite). Of these different mechanisms, the hydration and swelling of clay minerals have been considered to be the most important one leading to the weakening and instability of the shale rock. From the quantitative mineralogy analysis (Table 1), the studied shale sample contains 10.0 wt % illite and 5.2 wt % chlorite, which can interact with water due to their physico-chemically active surfaces and the adsorbed cations therein. While no expandable layers (e.g., smectite, vermiculite) are present in this shale, osmotic swelling of clay minerals, but no interlayer swelling, still takes place, which usually results from the difference in cation concentrations of the pore fluid close to the clay surface and of the bulk pore fluid (Madsen and Müller-Vonmoos 1989). Prior studies have shown that the swelling of clay minerals induced by either interlayer expansion or osmotic swelling may force clay particles partially separate from each other (i.e., slaking) and hence reduce the contact areas among particles when subjected to external loads, thereby reducing the mechanical properties of the rock (Amorim et al. 2007; Yuan et al. 2014).

The electrical double layer (EDL) repulsion induced by the fracturing fluid–clay interactions is another factor contributing to shale softening. The EDL thickness of clays (e.g., Na-smectite in distilled water) can be quite significant compared to the size of pores and cracks in shale (Mojid and Cho 2006), which can give rise to unfavorable electrostatic repulsion between particles as well as increased pressure to the pores and cracks in shale (Du et al. 2018). Moreover, as a sedimentary rock, the mechanical properties of shale are also strongly influenced by surface forces (e.g., van der Waals forces, solid–solid bonds or cementations) between particle contacts, which can also be altered or broken by shale–fluid interactions (Boozer et al. 1963; Spencer 1981; Murphy et al. 1986; Tutuncu and Sharma 2002; Tutuncu et al. 2002). In addition, the liquid infiltrated into shale is able to act as a lubricant and hence reduces the internal frictional resistance of mineral particles.

A peculiar mineral, pyrite, is usually found in various shale formations. Upon exposure to air, pyrite can be easily oxidized (Lowson 1982; Nordstrom 1982), leading to the formation of sulfuric acid, which can in turn dissolve carbonates, a typical cementation agent. Such an oxidization reaction is also usually accompanied by the generation of significant heat, causing thermal expansion and hence cracking of the rock (Nordstrom 1982; Rimstidt and Vaughan 2003). Although the studied shale only has a limited fraction of pyrite (e.g., 2.0 wt %), its oxidation can still cause calcite dissolution, and the thermal expansion may lead certain microcracking of the rock. Both processes can have a negative impact on the mechanical performance of the rock.

In summary, a variety of physical and chemical mechanisms contribute to the softening of shale rock. Under the combined effects of various factors discussed above, the mechanical properties of the clay matrix as well as the bulk shale are significantly reduced by prolonged hydrothermal treatment. All of these mechanisms require the presence of water (and air to a lesser extent). As such, the rate of softening advancement from the exterior surface to the interior of the rock is controlled by permeation of water through or inside the rock. Via the newly developed LV-based statistical nanoindentation, the softening rate is determined as 10.5 $\mu\text{m}/\text{day}$. Given that the coefficient of hydraulic conductivity of most shales ranges from 0.09 to 86.4 $\mu\text{m}/\text{day}$ (Neuzil 1994; Pope et al. 2009), it can be concluded that water permeation or infiltration basically dominates the rate of softening. This finding is of key interest to the petroleum industry because of its practical significance for the design and operation of oil/gas recovery projects.

4 Conclusions

In this paper, a newly developed large volume (LV)-based statistical nanoindentation technique was successfully employed to quantitatively characterize the shale softening

behavior. The mechanisms of softening, including the degree (i.e., as reflected by the change in Young's modulus) and rate of softening, are determined and analyzed by statistical analysis of massive experimental data as well as a newly proposed surround effect model. The main conclusions can be drawn as follows:

- CDF-based statistical deconvolution of the massive indentation data over large indentation depths (e.g., 6000 nm) combined with the surround effect model yields the determination of the mechanical properties of individual minerals at the nano- to micro-scales and the bulk rock at the macroscale, i.e., the cross-scale characterization of the mechanical properties of the rock.
- LV-based indentation measurements, achieved by sacrificial removal of the prior indented layers, can uncover the extend of shale softening, as reflected by the magnitude of reduction in the Young's modulus of the individual phases and bulk rock, as well as the rate of softening advancement, which is controlled by the intrinsic permeability of the rock.
- The LV-based indentation technique is of practical importance, and can be implemented as a viable protocol for screening and optimizing various chemical stimulants and additives used in hydraulic fracturing and oil/gas production operations.
- This technique opens new paradigms to study the mechanical properties of shales as well as how shales undergo dynamic changes during hydraulic fracturing and oil/gas extraction processes, and it can be implemented as a protocol for screening and optimizing chemical stimulants and additives used in oil/gas production operations.
- This technique opens new paradigms to study the mechanical properties of shales as well as how shales undergo dynamic changes during hydraulic fracturing and oil/gas extraction processes, and it can be implemented as a protocol for screening and optimizing chemical stimulants and additives used in oil/gas production operations.

Acknowledgements This work was partially supported by the National Natural Science Foundation of China (Grant No. 51774305) and Major Projects of the National Natural Science Foundation of China (Grant No. 51490651).

References

Ahmadov R, Vanorio T, Mavko G (2009) Confocal laser scanning and atomic-force microscopy in estimation of elastic properties of the organic-rich Bazhenov Formation. *Lead Edge* 28:18–23

- Akrad OM, Miskimins JL, Prasad M (2011) The effects of fracturing fluids on shale rock mechanical properties and proppant embedment. *SPE Annu Tech Conf, Exhib*, p 12
- Alramahi B, Sundberg MI (2012) Proppant embedment and conductivity of hydraulic fractures in shales. In: 46th U.S. rock mechanics/geomechanics symposium. american rock mechanics association, Chicago, p 6
- Amorim CLG, Lopes RT, Barroso RC et al (2007) Effect of clay–water interactions on clay swelling by X-ray diffraction. *Nucl Instrum Methods Phys Res* 580:768–770. <https://doi.org/10.1016/j.nima.2007.05.103>
- Anderson RL, Ratcliffe I, Greenwell HC et al (2010) Clay swelling - A challenge in the oilfield. *Earth Sci Rev* 98:201–216. <https://doi.org/10.1016/j.earscirev.2009.11.003>
- Baihly JD, Altman RM, Malpani R, Luo F (2010) Shale gas production decline trend comparison over time and basins. In: SPE annual technical conference and exhibition. Society of Petroleum Engineers, Florence
- Bennett KC, Berla LA, Nix WD, Borja RI (2015) Instrumented nanoindentation and 3D mechanistic modeling of a shale at multiple scales. *Acta Geotech* 10:1–14. <https://doi.org/10.1007/s11440-014-0363-7>
- Bobko C, Ulm FJ (2008) The nano-mechanical morphology of shale. *Mech Mater* 40:318–337. <https://doi.org/10.1016/j.mechmat.2007.09.006>
- Boozer GD, Hiller KH, Serdengecti S (1963) Effects of pore fluids on the deformation behavior of rocks subjected to triaxial compression. *Proc fifth symp rock mech. Univ Minnesota*, 579–624. <https://doi.org/10.3390/pr6080107>
- Chandra AP, Gerson AR (2010) The mechanisms of pyrite oxidation and leaching: a fundamental perspective. *Surf Sci Rep* 65:293–315. <https://doi.org/10.1016/j.surfrep.2010.08.003>
- Chenevert ME (1970) Shale control with balanced-activity oil-continuous muds. *J Pet Technol* 22:1309–1316. <https://doi.org/10.2118/2559-PA>
- Constantinides G, Ravi Chandran KS, Ulm FJ, Van Vliet KJ (2006) Grid indentation analysis of composite microstructure and mechanics: principles and validation. *Mater Sci Eng, A* 430:189–202. <https://doi.org/10.1016/j.msea.2006.05.125>
- DeJong MJ, Ulm FJ (2007) The nanogranular behavior of C-S-H at elevated temperatures (up to 700 °C). *Cem Concr Res* 37:1–12. <https://doi.org/10.1016/j.cemconres.2006.09.006>
- Doebelin N, Kleeberg R (2015) Profex: a graphical user interface for the Rietveld refinement program BGMN. *J Appl Crystallogr* 48:1573–1580. <https://doi.org/10.1107/S1600576715014685>
- Doerner MF, Nix WD (1986) A method for interpreting the data from depth-sensing indentation instruments. *J Mater Res* 1:601–609. <https://doi.org/10.1557/JMR.1986.0601>
- Du J, Hu L, Meegoda JN, Zhang G (2018) Shale softening: observations, phenomenological behavior, and mechanisms. *Appl Clay Sci* 161:290–300. <https://doi.org/10.1016/j.clay.2018.04.033>
- Eliyahu M, Emmanuel S, Day-Stirrat RJ, Macaulay CI (2015) Mechanical properties of organic matter in shales mapped at the nanometer scale. *Mar Pet Geol* 59:294–304. <https://doi.org/10.1016/j.marpetgeo.2014.09.007>
- Fischer-Cripps AC (2007) Illustrative analysis of load-displacement curves in nanoindentation. *J Mater Res* 22:3075–3086. <https://doi.org/10.1557/jmr.2007.0381>
- Giger FM, Reiss LH, Jourdan AP (1984) The reservoir engineering aspects of horizontal drilling. In: SPE annual technical conference and exhibition. Society of Petroleum Engineers, Houston, p 8
- Guo X, Liu K, He S et al (2012) Petroleum generation and charge history of the northern Dongying Depression, Bohai Bay Basin, China: insight from integrated fluid inclusion analysis and basin modelling. *Mar Pet Geol* 32:21–35. <https://doi.org/10.1016/j.marpetgeo.2011.12.007>

- Hu Y, Devegowda D, Sigal R (2016) A microscopic characterization of wettability in shale kerogen with varying maturity levels. *J Nat Gas Sci Eng* 33:1078–1086. <https://doi.org/10.1016/j.jngse.2016.06.014>
- Huang R, Wang Y, Cheng S, Liu S, Cheng L (2015) Selection of logging-based TOC calculation methods for shale reservoirs: a case study of the Jiaoshiba shale gas field in the Sichuan Basin. *Nat Gas Ind B* 2(2–3):155–161
- Huitt JL, Mcglothlin Jr. BB (1958) The propping of fractures in formations susceptible to propping-sand embedment. In: *Drilling and production practice*. American Petroleum Institute, New York, p 9
- Johnson KL (1985) *Contact mechanics*. Cambridge University Press, Cambridge
- Khodja M, Canselier JP, Bergaya F et al (2010) Shale problems and water-based drilling fluid optimisation in the Hassi Messaoud Algerian oil field. *Appl Clay Sci* 49:383–393. <https://doi.org/10.1016/j.clay.2010.06.008>
- King GE (2010) Thirty years of gas shale fracturing: what have we learned? In: *SPE Annual Technical Conference and Exhibition*, Florence
- King GE (2012) Hydraulic fracturing 101: what every representative, environmentalist, regulator, reporter, investor, university researcher, neighbor, and engineer should know about hydraulic fracturing risk. *J Pet Technol* 64:34–42. <https://doi.org/10.2118/0412-0034-JPT>
- Kuila U, McCarty DK, Derkowski A et al (2014) Nano-scale texture and porosity of organic matter and clay minerals in organic-rich mudrocks. *Fuel* 135:359–373. <https://doi.org/10.1016/j.fuel.2014.06.036>
- LaFollette RF, Carman PS (2010) Proppant diagenesis: results so far. In: *SPE Unconventional Gas Conference*. Society of Petroleum Engineers, Pittsburgh, p 14
- Leisen D, Kerkamm I, Bohn E, Kamlah M (2012) A novel and simple approach for characterizing the Young's modulus of single particles in a soft matrix by nanoindentation. *J Mater Res* 27:3073–3082. <https://doi.org/10.1557/jmr.2012.391>
- Lin S, Lai B (2013) Experimental investigation of water saturation effects on Barnett shale's geomechanical behaviors. In: *SPE annual technical conference and exhibition*. Society of Petroleum Engineers, New Orleans, p 10
- Locock AJ, Chesterman D, Caird D, Duke MJM (2012) Miniaturization of mechanical milling for powder X-ray diffraction. *Powder Diffr* 27:189–193. <https://doi.org/10.1017/S0885715612000516>
- Lowson RT (1982) Aqueous oxidation of pyrite by molecular oxygen. *Chem Rev* 82:461–497. <https://doi.org/10.1021/cr00051a001>
- Lu Y, Zeng L, Xie Q, Jin Y, Hossain MM, Saeedi A (2019) Analytical modelling of wettability alteration-induced micro-fractures during hydraulic fracturing in tight oil reservoirs. *Fuel* 249:434–440
- Madsen FT, Müller-Vonmoos M (1989) The swelling behaviour of clays. *Appl Clay Sci* 4:143–156. [https://doi.org/10.1016/0169-1317\(89\)90005-7](https://doi.org/10.1016/0169-1317(89)90005-7)
- Menčík J, Munz D, Quandt E et al (1997) Determination of elastic modulus of thin layers using nanoindentation. *J Mater Res* 12:2475–2484. <https://doi.org/10.1557/JMR.1997.0327>
- Mesarovic SDJ, Fleck NA (1999) Spherical indentation of elastic-plastic solids. *Proc R Soc A Math Phys Eng Sci* 455:2707–2728. <https://doi.org/10.1098/rspa.1999.0423>
- Miller M, Bobko C, Vandamme M, Ulm FJ (2008) Surface roughness criteria for cement paste nanoindentation. *Cem Concr Res* 38:467–476. <https://doi.org/10.1016/j.cemconres.2007.11.014>
- Minh DN, Gharbi H, Rejeb A, Vale F (2004) Experimental study of the influence of the degree of saturation on physical and mechanical properties in Tournemire shale (France). *Appl Clay Sci* 26:197–207. <https://doi.org/10.1016/j.clay.2003.12.032>
- Mojid MA, Cho H (2006) Estimating the fully developed diffuse double layer thickness from the bulk electrical conductivity in clay. *Appl Clay Sci* 33:278–286. <https://doi.org/10.1016/j.clay.2006.06.002>
- Moore DM, Reynolds RC (1997) *X-Ray diffraction and the identification and analysis of clay minerals*. Oxford Univ Press, Oxford
- Murphy WF III, Winkler KW, Kleinberg RL (1986) Acoustic relaxation in sedimentary rocks: dependence on grain contacts and fluid saturation. *Geophysics* 51:757–766. <https://doi.org/10.1190/1.1442128>
- Neuzil CE (1994) How permeable are clays and shales? *Water Resour Res* 30:145–150. <https://doi.org/10.1029/93WR02930>
- Nordstrom DK (1982) Aqueous pyrite oxidation and the consequent formation of secondary iron minerals. In: *Acid Sulfate Weathering*. Fort Collins
- Oliver WC, Pharr GM (1992) An improved technique for determining hardness and elastic modulus using load and displacement sensing indentation experiments. *J Mater Res* 7:1564–1583. <https://doi.org/10.1557/JMR.1992.1564>
- Oliver WC, Pharr GM (2004) Measurement of hardness and elastic modulus by instrumented indentation: advances in understanding and refinements to methodology. *J Mater Res* 19:3–20. <https://doi.org/10.1557/jmr.2004.19.1.3>
- Pimentel E (2003) Swelling behaviour of sedimentary rocks under consideration of micromechanical aspects and its consequences on structure design. In: *Geotechnical measurements and modelling*. Karlsruhe, pp 367–374
- Pope C, Peters B, Benton T, Palisch T (2009) Haynesville shale—One operator's approach to well completions in this evolving play. In: *SPE annual technical conference and exhibition*. Society of Petroleum Engineers, New Orleans, p 12
- Rickman R, Mullen MJ, Petre JE, et al (2008) A practical use of shale petrophysics for stimulation design optimization: All shale plays are not clones of the Barnett shale. In: *SPE annual technical conference and exhibition*. Denver
- Rimstidt DD, Vaughan DJ (2003) Pyrite oxidation: a state-of-the-art assessment of the reaction mechanism. *Geochim Cosmochim Acta* 67:873–880. [https://doi.org/10.1016/S0016-7037\(02\)01165-1](https://doi.org/10.1016/S0016-7037(02)01165-1)
- Saha R, Nix WD (2002) Effects of the substrate on the determination of thin film mechanical properties by nanoindentation. *Acta Mater* 50:23–38. [https://doi.org/10.1016/S1359-6454\(01\)00328-7](https://doi.org/10.1016/S1359-6454(01)00328-7)
- Salmon V, Derenne S, Lallier-Vergès E et al (2000) Protection of organic matter by mineral matrix in a Cenomanian black shale. *Org Geochem* 31:463–474. [https://doi.org/10.1016/S0146-6380\(00\)00013-9](https://doi.org/10.1016/S0146-6380(00)00013-9)
- Speight JG (2005) *Lange's handbook of chemistry*. McGraw-Hill, Laramie
- Spencer JW (1981) Stress relaxations at low frequencies in fluid-saturated rocks: attenuation and modulus dispersion. *J Geophys Res Solid Earth* 86:1803–1812. <https://doi.org/10.1029/JB086iB03p01803>
- Sun Y, Aman M, Espinoza DN (2016) Assessment of mechanical rock alteration caused by CO₂-water mixtures using indentation and scratch experiments. *Int J Greenh Gas Control* 45:9–17. <https://doi.org/10.1016/j.ijggc.2015.11.021>
- Terracina JM, Turner JM, Collins DH, Spillars S (2010) Proppant selection and its effect on the results of fracturing treatments performed in shale formations. In: *SPE annual technical conference and exhibition*. Society of Petroleum Engineers, Florence, p 17
- Tsui TY, Pharr GM (1999) Substrate effects on nanoindentation mechanical property measurement of soft films on hard substrates. *J Mater Res* 14:292–301. <https://doi.org/10.1557/JMR.1999.0042>
- Tutuncu AN, Sharma MM (2002) The influence of fluids on grain contact stiffness and frame moduli in sedimentary rocks. *Geophysics* 57:1571–1582. <https://doi.org/10.1190/1.1443225>

- Tutuncu AN, Podio AL, Sharma MM (2002) Nonlinear viscoelastic behavior of sedimentary rocks, Part II: hysteresis effects and influence of type of fluid on elastic moduli. *Geophysics* 63:195–203. <https://doi.org/10.1190/1.1444313>
- Ulm F-J, Abousleiman Y (2006) The nanogranular nature of shale. *Acta Geotech* 1:77–88. <https://doi.org/10.1007/s11440-006-0009-5>
- Ulm FJ, Vandamme M, Bobko C et al (2007) Statistical indentation techniques for hydrated nanocomposites: concrete, bone, and shale. *J Am Ceram Soc* 90:2677–2692. <https://doi.org/10.1111/j.1551-2916.2007.02012.x>
- Valès F, Nguyen Minh D, Gharbi H, Rejeb A (2004) Experimental study of the influence of the degree of saturation on physical and mechanical properties in Tournemire shale (France). *Appl Clay Sci* 26:197–207. <https://doi.org/10.1016/j.clay.2003.12.032>
- Wei Z, Zhang G, Chen H et al (2009) A simple method for evaluating elastic modulus of thin films by nanoindentation. *J Mater Res* 24:801–815. <https://doi.org/10.1557/jmr.2009.0109>
- Wong R (1998) Swelling and softening behaviour of La Biche shale. *Can Geotech J* 35:206–221. <https://doi.org/10.1139/t97-087>
- Yang Z, Wang L, Chen Z et al (2018) Micromechanical characterization of fluid/shale interactions by means of nanoindentation. *SPE Reserv Eval Eng* 21:405–417. <https://doi.org/10.2118/181833-PA>
- Yuan W, Li X, Pan Z et al (2014) Experimental investigation of interactions between water and a lower silurian Chinese shale. *Energy Fuels* 28:4925–4933. <https://doi.org/10.1021/ef500915k>
- Zhang G, Germaine JT, Martin RT, Whittle AJ (2003) A simple sample-mounting method for random powder X-ray diffraction. *Clays Clay Miner* 51:218–225. <https://doi.org/10.1346/CCMN.2003.0510212>
- Zhou Z, Abass H, Li X et al (2016) Mechanisms of imbibition during hydraulic fracturing in shale formations. *J Pet Sci Eng* 141:125–132. <https://doi.org/10.1016/J.PETROL.2016.01.021>
- Zhu W, Hughes JJ, Bicanic N, Pearce CJ (2007) Nanoindentation mapping of mechanical properties of cement paste and natural rocks. *Mater Charact* 58:1189–1198. <https://doi.org/10.1016/j.matchar.2007.05.018>

Publisher's Note Springer Nature remains neutral with regard to jurisdictional claims in published maps and institutional affiliations.